Universiteit
Leiden
The Netherlands

Transformation and sublimation of interstellar ices: insights from laboratory experiments and astronomical observations

Carvalho Santos, J. de

Citation

Carvalho Santos, J. de. (2025, July 2). *Transformation and sublimation of interstellar ices: insights from laboratory experiments and astronomical observations*. Retrieved from https://hdl.handle.net/1887/4252309

Version:	Publisher's Version
License:	Licence agreement concerning inclusion of doctoral thesis in the Institutional Repository of the University of Leiden
Downloaded from:	https://hdl.handle.net/1887/4252309

Note: To cite this publication please use the final published version (if applicable).

5. H_2S ICE SUBLIMATION DYNAMICS: EXPERIMENTALLY CONSTRAINED BINDING ENERGIES, ENTRAPMENT EFFICIENCIES, AND SNOWLINES

Hydrogen sulfide (H_2S) is thought to be an important sulfur reservoir in interstellar ices. It serves as a key precursor to complex sulfur-bearing organics, and has been proposed to play a significant role in the origin of life. Although models and observations both suggest H_2S to be present in ices in non-negligible amounts, its sublimation dynamics remain poorly constrained. In this work, we present a comprehensive experimental characterization of the sublimation behavior of H_2S ice under astrophysically-relevant conditions. We used an ultrahigh vacuum chamber to deposit pure multilayer H_2S ice, submonolayer H_2S ice on top of compact amorphous solid water (cASW), as well as ice mixtures of H_2S and H_2O. The sublimation behavior of H_2S was monitored with a quadrupole mass spectrometer (QMS) during temperature-programmed desorption (TPD) experiments. These experiments are used to determine binding energies and entrapment efficiencies of H_2S, which are then employed to estimate its snowline positions in a protoplanetary disk midplane. We derive mean binding energies of 3159 ± 46 K for pure H_2S ice and 3392 ± 56 K for submonolayer H_2S desorbing from a cASW surface. These values correspond to sublimation temperatures of around 64 K and 69 K in the disk midplane, placing its sublimation fronts at radii just interior to the CO_2 snowline. We also investigate the entrapment of H_2S in water ice and find it to be highly efficient, with $\sim 75 - 85\%$ of H_2S remaining trapped past its sublimation temperature for H_2O:H_2S mixing ratios of $\sim$5$-$17:1. We discuss potential mechanisms behind this efficient entrapment. Our findings imply that, in protoplanetary disks, H_2S will mostly be retained in the ice phase until water crystallizes, at radii near the water snowline, if it forms mixed into water ice. This has significant implications for the possibility of H_2S being incorporated into icy planetesimals and its potential delivery to terrestrial planets, which we discuss in detail.

J. C. Santos, E. L. Piacentino, J. B. Bergner, M. Rajappan, K. I. Öberg. 2025, *in press.*

5.1 Introduction

The interchange between solids and gas plays a major role in the chemical composition and structure of star- and planet-forming regions (Bergin & Langer 1997; Aikawa *et al.* 2002; Viti *et al.* 2004; Henning & Semenov 2013; He *et al.* 2016b; Öberg *et al.* 2023). At the cold temperatures of interstellar clouds (typically $\sim$10$-$20 K), most molecules adsorb onto dust grains, forming ice mantles that undergo rich solid-state chemical processes. The result is a lavish icy chemical reservoir—spanning from simple molecules such as CO and H_2O to complex organics (Herbst & van Dishoeck 2009; van Dishoeck 2014; Linnartz *et al.* 2015; Öberg 2016; Cuppen *et al.* 2024). As this interstellar material collapses into an emerging young stellar object, increasing temperatures caused by the heat from the protostar enable the diffusion of ice species—further facilitating chemical reactions (see, e.g., Cuppen *et al.* 2017)—and eventually lead to their thermal sublimation. The locations of these sublimation fronts, or snowlines, determine the physical state in which specific molecules are available for incorporation into forming planets and planetesimals, thus shaping their solid and atmospheric constitution (Öberg *et al.* 2011b; Henning & Semenov 2013; Madhusudhan 2019). Such locations are dictated by a combination of desorption kinetics, set by a species' binding energies, and the efficiencies with which it is trapped within less volatile ice matrices. It is thus paramount to characterize the thermal sublimation behavior of ice species in order to understand the chemical evolution of environments where young solar system bodies are forming.

One particularly riveting volatile interstellar molecule is hydrogen sulfide (H_2S). Following its first detection by Thaddeus *et al.* (1972) in seven Galactic sources, it has since been observed in the gas phase towards a range of interstellar and protoplanetary environments: from clouds (Minh *et al.* 1989; Neufeld *et al.* 2015) to dense cores and protostars (Minh *et al.* 1990; van Dishoeck *et al.* 1995; Hatchell *et al.* 1998; Vastel *et al.* 2003; Wakelam *et al.* 2004) to protoplanetary disks (Phuong *et al.* 2018; Rivière-Marichalar *et al.* 2021, 2022). On the other hand, interstellar H_2S ice has yet to be observed, with abundance upper limits in prestellar cores and protostellar envelopes estimated as $\lesssim$1% with respect to H_2O (Smith 1991; Jiménez-Escobar & Muñoz Caro 2011a; McClure *et al.* 2023). This non-detection is likely associated with the intrinsic limitations of astronomical observations in the solid state (e.g., the broadness of the ice features and their high degeneracy). Indeed, the strongest IR feature of H_2S ice (its S-H stretching modes at 3.93 μm) is particularly challenging to unequivocally observe due to its broad profile and because it overlaps both with CH_3OH combination modes (a major ice component) and with the S-H stretching modes of simple thiols (Jiménez-Escobar & Muñoz Caro 2011a; Hudson & Gerakines 2018). While the latter are less concerning due to the low expected abundances of thiols, both factors still complicate confidently assigning absorption features in this region to H_2S. Nevertheless, H_2S is predicted by chemical models to be very efficiently formed in ices via the successive hydrogenation of S atoms (see, e.g., Garrod *et al.* 2007; Druard & Wakelam 2012; Esplugues *et al.* 2014; Vidal *et al.* 2017; Vidal & Wakelam 2018):

$$\mathrm{S} \xrightarrow{+\mathrm{H}} \mathrm{HS} \xrightarrow{+\mathrm{H}} \mathrm{H_2S}. \tag{5.1}$$

Indeed, it has been observed to be a major sulfur carrier in the comae of comets (Mumma *et al.* 2011; Le Roy *et al.* 2015; Biver *et al.* 2015; Calmonte *et al.* 2016), which are thought to (at least partially) inherit the ice material from the prior pre- and protostellar evolutionary stages (e.g., Bockelée-Morvan *et al.* 2000a; Altwegg *et al.* 2017; Rubin *et al.* 2018; Drozdovskaya *et al.* 2019). Cometary H_2S abundances relative to H_2O range between $\sim$0.13$-$1.75% (Calmonte *et al.* 2016 and references therein), with measurements from the coma of comet 67P/Churymov-Gerasimenko (hereafter 67P) by the Rosetta Orbiter Sensors for Ion and Neutral Analysis (ROSINA) instrument on board of the Rosetta spacecraft yielding H_2S/H_2O abundances of 1.06 ± 0.05% (Calmonte *et al.* 2016). These findings point to H_2S as the

main volatile sulfur carrier in 67P. Consequently, while the upper limits on H_2S ice are sufficient to rule it out as the main interstellar sulfur reservoir (see, e.g., Jiménez-Escobar & Muñoz Caro 2011a), cometary inheritance from interstellar ices remains a plausible hypothesis within current observational constraints. Moreover, observed gas-phase H_2S abundances toward solar-mass protostars—attributed to the sublimation of ices in the hot core region—suggest H_2S to be an important gaseous sulfur carrier (Drozdovskaya *et al.* 2018). Given that gas-phase routes to H_2S cannot account for its detected gaseous abundances, all evidence point to it being present in interstellar ices at a level of $\sim$1% with respect to H_2O.

Irrespective of its physical state, H_2S can serve as a important source of sulfur during the chemical evolution of star- and planet-forming regions. As a solid, it has been shown both experimentally and by chemical models to initiate a prolific sulfur network by producing HS radicals and S atoms—induced either by energetic processing or interactions with H atoms—that readily react with other ice species (Moore *et al.* 2007; Ferrante *et al.* 2008; Garozzo *et al.* 2010; Jiménez-Escobar *et al.* 2014a; Chen *et al.* 2015; Laas & Caselli 2019; Santos *et al.* 2024a,b). Solid H_2S and its reaction products might then be incorporated into icy planetesimals, which in turn might deliver them to terrestrial planets during events such as our Solar System's late heavy bombardments. This is particularly relevant to theories on the origins of life, as H_2S has been proposed as a key energy source for early metabolic pathways predating oxygenic photosynthesis (Olson & Straub 2016). More broadly, sulfur-bearing compounds have long been recognized as fundamental to biological systems. Additionally, H_2S can also undergo solid-state acid-base reactions with NH_3 to form ammonium hydrosulfide ($NH_4^+SH^-$) at temperatures as low as 10 K (Loeffler *et al.* 2015; Vitorino *et al.* 2024; Slavicinska *et al.* 2025). This salt has been detected at very high abundances in the grains of comet 67P by the ROSINA instrument (Altwegg *et al.* 2022), and is proposed to be a major carrier of the 6.85 μm band assigned to NH_4^+ in ices, as well as a significant sink to the conspicuous missing sulfur problem (Slavicinska *et al.* 2025). As a gas, H_2S can contribute to the elemental abundance of sulfur in planetary atmospheres—which in turn might help tracing the planet's formation history (Öberg *et al.* 2011b; Polman *et al.* 2023; Tsai *et al.* 2023).

Despite its pivotal role in the sulfur network of star- and planet-forming regions, a comprehensive characterization of the thermal sublimation behavior of H_2S is still lacking from the literature, with no experimentally-determined binding energies or entrapment efficiencies available to date. We aim to bridge this gap with this work. The paper is outlined as follows: in Section 5.2, the experimental setup and procedures are described. In section 5.3, we report and discuss our results, including experimentally-derived binding energies as well as entrapment efficiencies in H_2O ice. The corresponding locations of the H_2S sublimation fronts and their astrophysical implications are discussed in Section 5.4. Finally, in Section 5.5 we summarize our main findings.

5.2 Methods

5.2.1 The setup

This work utilized the experimental setup SPACE-KITTEN[1], which has been described in detail elsewhere (Simon *et al.* 2019, 2023). Briefly, the setup consists of an ultrahigh vacuum (UHV) chamber with base pressure at room temperature of $\sim 4\times10^{-9}$ Torr. At the center of the chamber, an IR-transparent CsI window is mounted on a sample holder attached to a closed-cycle helium cryostat with a DMX-20B interface (which decouples the sample holder from the cryostat's cold tip, thus preventing vibrations). The substrate temperature can be varied between 12 and 300 K using a resistive thermofoil heater, and is monitored by

[1]Surface Processing Apparatus for Chemical Experimentation–Kinetics of Ice Transformation in Thermal ENvironments

two silicon diode sensors with a precision of ±0.1 K and absolute accuracy of ∼2 K. H_2S (Sigma-Aldrich, purity ≥99.5%) and H_2O are admitted into the chamber, either individually or as a mixture, through a stainless steel tube doser with a diameter of 4.8 mm at normal incidence to the substrate. The doser outlet is located at 1 inch from the substrate during deposition and the base pressure of the gas line is $\sim 10^{-4}$ Torr. The H_2O sample was prepared by purifying deionized water through multiple freeze-pump-thaw cycles in a liquid nitrogen bath. Moreover, $^{13}CO_2$ (Sigma-Aldrich, purity 99%; <3 atom % ^{18}O, 99 atom % ^{13}C) is also utilized for a control experiment mixed with H_2O. The minor isotopologue is chosen to avoid any potential residual atmospheric contamination from interfering with the analysis. Ice growth is monitored by a Bruker Optics Vertex 70 Fourier-transform infrared spectrometer (FTIR) in transmission mode, while the gas-phase composition in the chamber is sampled by a Pfeiffer Vaccum Inc. PrismaPlus QMG 220 quadrupole mass spectrometer (QMS).

5.2.2 The experiments

The experiments performed in this work are summarized in Table 5.1. We derive binding energies of H_2S in two scenarios: for pure multilayer H_2S ice and for submonolayer H_2S on top of multilayer compact amorphous solid water (cASW). The latter was chosen as a substrate because it is generally thought to be more representative of interstellar water ice than porous counterparts (e.g., Accolla *et al.* 2013). In order to grow cASW, the substrate is kept at 100 K during the H_2O ice deposition (Bossa *et al.* 2012), and is subsequently cooled down to 15 K before depositing H_2S. The pure multilayer H_2S ices are deposited at 15 K directly. Entrapment experiments are performed for water-dominated ice mixtures of H_2S or $^{13}CO_2$ deposited at 15 K. Prior to dosing, the mixtures are prepared in a gas manifold within one hour of the experiment. In all cases, after the deposition is completed, temperature programmed desorption (TPD) experiments are performed by heating up the substrate temperature linearly at a rate of 2 K min^{-1}. The desorbed species are immediately ionized by 70 eV electron impact and are monitored by the QMS. Their desorption rates are then used to derive the binding energies and entrapment efficiencies. Any contamination from background H_2O deposition is negligible. Based on the infrared absorption features of H_2O observed after H_2S deposition in the pure ice experiments, the background H_2O deposition rate is at most 0.1 ML/min. This is at least one order of magnitude lower than the H_2S deposition rate in the multilayer experiments and a factor of ∼5 lower in the submonolayer experiments. Even in the latter case, we find no evidence of significant H_2O codeposition with H_2S, as no additional desorption feature is observed with the QMS following the submonolayer desorption of H_2S—which would be expected if a non-negligible amount of porous ASW were forming due to background deposition at 15 K.

The surface coverage of the ice species is quantified by two approaches. For ices with thicknesses $\gtrsim$1 ML, taken as the typical approximation of 1 ML = 10^{15} molecules cm^{-2}, their infrared absorbance bands are reliably detected above the instrumental limit of the spectrometer. In such cases, the IR integrated absorbance ($\int Abs(\tilde{\nu})d\nu$) of the species is converted to absolute abundance using a modified Beer-Lambert law:

$$N_X = \ln 10 \frac{\int Abs(\tilde{\nu})\mathrm{d}\tilde{\nu}}{A(X)}, \tag{5.2}$$

where N_X is the species' column density in molecules cm^{-2} and $A(X)$ is its absorption band strength in cm $molecule^{-1}$. We use $A(H_2S)_{\text{S-H str}} = 1.69 \times 10^{-17}$ cm $molecule^{-1}$ for pure H_2S ices and $A(H_2S)_{\text{S-H str}} = 1.66 \times 10^{-17}$ cm $molecule^{-1}$ for H_2S mixed with H_2O, as derived by Yarnall & Hudson (2022). For H_2O and $^{13}CO_2$, we use $A(H_2O)_{\text{O-H str}} = 2.2 \times 10^{-16}$ cm $molecule^{-1}$ and $A(^{13}CO_2)_{\text{C=O str}} = 1.15 \times 10^{-16}$ cm $molecule^{-1}$, taken from Bouilloud *et al.* (2015) based on the values reported by Gerakines *et al.* (1995). Uncertainties in the band strengths are the main source of error in the ice coverage estimation, and are assumed

Table 5.1: List of experiments.

Experiment[a]	X coverage (ML)	H_2O coverage (ML)	Total mixture coverage (ML)	H_2O:X
		X = H_2S		
H_2S	90	–	–	–
H_2S	73	–	–	–
H_2S	45	–	–	–
H_2S	32	–	–	–
H_2S	19	–	–	–
H_2O→H_2S	1.6	42	–	–
H_2O→H_2S	1.2	40	–	–
H_2O→H_2S	0.6	40	–	–
H_2O→H_2S	0.5	39	–	–
H_2O→H_2S	0.3	39	–	–
H_2O→H_2S	0.2	47	–	–
H_2O:H_2S	7.0	36	43.0	5.1:1
H_2O:H_2S	5.1	38	43.1	7.5:1
H_2O:H_2S	4.2	39	43.2	9.3:1
H_2O:H_2S	2.3	40	42.3	17:1
		X = $^{13}CO_2$		
H_2O:$^{13}CO_2$	2.6	37	39.6	14:1

Notes. [(a)] Arrows (H_2O→X) denote sequential depositions (X on top of H_2O); colons (H_2O:X) denote ice mixtures of H_2O and X.

to be 10% to account for possible variations caused by temperature and mixing conditions. This uncertainty is then propagated throughout the analysis. For the cases in which ices are deposited with submonolayer coverages, IR absorption bands are not or barely detected and the coverage is estimated by the species' integrated QMS signal during TPD corrected by a scaling factor (see Appendix 5.7.1 for more details).

5.2.3 The analysis

The H_2S binding energies are derived by fitting the measured TPD curves with the Polanyi-Wigner equation:

$$-\frac{d\theta}{dT} = \frac{\nu}{\beta}\theta^n e^{-E_{\rm des}/T}, \tag{5.3}$$

where θ is the ice coverage in monolayers, T is the ice temperature in K, β is the heating rate in K s^{-1}, ν is the preexponential factor, n is the kinetic order, and $E_{\rm des}$ is the desorption energy in K. The kinetic order is a dimensionless quantity that indicates the influence of the species' concentration on its desorption rate. In the multilayer regime, desorption is independent of the ice thickness ($n = 0$), whereas in the submonolayer regime it is proportional to the ice coverage ($n = 1$). This reflects the constant number of adsorbates available for desorption at any given time in the former case, as opposed to the varying number in the latter. The preexponential factor is associated with the molecule's frequency of vibration in the adsorbate−surface potential well, and its units depend on the kinetic order (ML^{1-n} s^{-1}). For a given temperature T, we derive the preexponential factor following the transition state theory (TST) approach and approximating the partition function of the species in the adsorbed state to unity (that is, assuming it to be fully immobile; Tait *et al.* 2005; Minissale *et al.* 2022):

$$\nu_{\rm TST} = \frac{k_{\rm B}T}{h} q^{\ddagger}_{\rm tr,2D} q^{\ddagger}_{\rm rot,3D}. \tag{5.4}$$

Where $k_{\rm B}$ is the Boltzmann constant, h is the Planck constant, and $q^{\ddagger}_{\rm tr,2D}$ and $q^{\ddagger}_{\rm rot,3D}$ are the transitions state's partition functions of translation and rotation, respectively. All constants used here are in the MKS unit system. The translational motion perpendicular to the surface can be neglected, resulting in a translational partition functional parallel to the surface plane:

$$q^{\ddagger}_{\rm tr,2D} = \frac{A_S 2\pi m k_{\rm B} T}{h^2}, \tag{5.5}$$

where m is the mass of the species in kg and A_S is the surface area per adsorbed molecule, fixed to the typical value of 10^{-19} m^2. The rotational partition function is given by:

$$q^{\ddagger}_{\rm rot,3D} = \frac{\sqrt{\pi}}{\sigma h^3}(8\pi^2 k_{\rm B} T)^{3/2}\sqrt{I_x I_y I_z}, \tag{5.6}$$

where σ is the species' symmetry number (i.e., the number of indistinguishable rotated positions) and $I_x I_y I_z$ is the product of its principal moments of inertia. The choice of T values used to derive $\nu_{\rm TST}$ will be discussed in Sections 5.3.1.1 and 5.3.1.2 for their respective coverage regimes, while the rest of the parameters employed in equations 5.5 and 5.6 are listed in Table 5.2. The inertia moments of H_2S were calculated using Gaussian 16e (Frisch *et al.* 2016) at the M06-2X/aug-cc-pVTZ level of theory (Dunning Jr 1989; Zhao & Truhlar 2008a). The resulting $\nu_{\rm TST}$ are then used to fit equation 5.3 to the TPD curves and derive the corresponding binding energies.

When a more volatile species is embedded within a less volatile ice matrix, it can remain trapped in the solid phase beyond its expected sublimation temperature. The entrapment behavior of H_2S in H_2O-dominated ices is also investigated here, with $^{13}CO_2$ mixed into a water-rich ice included as a control experiment. As water ice crystallizes, it creates new

Table 5.2: Summary of parameters used to derive ν_{TST} for H_2S.

Parameter	Value
m (kg)	5.66×10^{-26}
σ	2
I_x (amu Å^2)	5.81066
I_y (amu Å^2)	6.71494
I_z (amu Å^2)	12.52560

Notes. See equations 5.4, 5.5, and 5.6.

channels that allow trapped species to reach the surface, producing the so-called "molecular volcano" desorption peaks (Smith *et al.* 1997). Entrapment efficiencies are calculated as the ratios of the integrated volcano-desorption TPD peak of the more volatile species (H_2S or $^{13}CO_2$) over the integrated area of its entire TPD curve. The integration bounds for the volcano peaks are defined by the temperature range of the water desorption peak, thus accounting for all volatiles sublimating concurrently with water. All mixed-ice experiments were conducted with a fixed total coverage of ∼40 ML to eliminate the influence of the ice thickness and isolate the effect of the mixing ratio on the entrapment efficiencies.

5.3 Results and discussion

5.3.1 Binding energies

5.3.1.1 H_2S–H_2S

Figure 5.1 shows the IR spectra obtained after completing the deposition of the pure H_2S ice in the multilayer experiments. The figure focuses on the frequency range of the S-H stretching modes of H_2S—its most prominent IR feature. Five different thicknesses (19, 32, 45, 73, and 90 ML) were used to derive the H_2S-H_2S binding energy; that is, the binding energy dominated by H_2S interactions with other H_2S molecules. The TPD curves for each coverage are shown in gray in Figure 5.2, measured from the mass-to-charge (m/z) ratio of 34, which corresponds to the molecular ion of H_2S and represents its dominant mass signal in electron-impact mass spectrometry at 70 eV ionization energy[2].

To fit the TPD curves with the Polanyi-Wigner equation (eq. 5.3), we must first determine the preexponential factor ν_{TST} of H_2S using equations 5.4, 5.5, and 5.6. Since these equations are temperature dependent, we opt to derive ν_{TST} at the maximum temperature where the experimental curve is still well described by an exponential behavior. This is to ensure consistency in the data analysis: by choosing the maximum temperature within the exponential range, we ensure that ν_{TST} is consistent with the region within which the model is fitted. This temperature is determined on the basis of its adjusted R^2 value, a coefficient that measures the proportion of variation in outcomes explained by the model, while adjusting for the number of predictors used. This adjustment is particularly important in this context, as R^2 naturally increases with the temperature, even without an improvement in model fit. The maximum temperatures are 79.2, 78.9, 80.5, 80.6, and 81.5 K for the respective coverages of 19, 32, 45, 73, and 90 ML.

[2]https://webbook.nist.gov

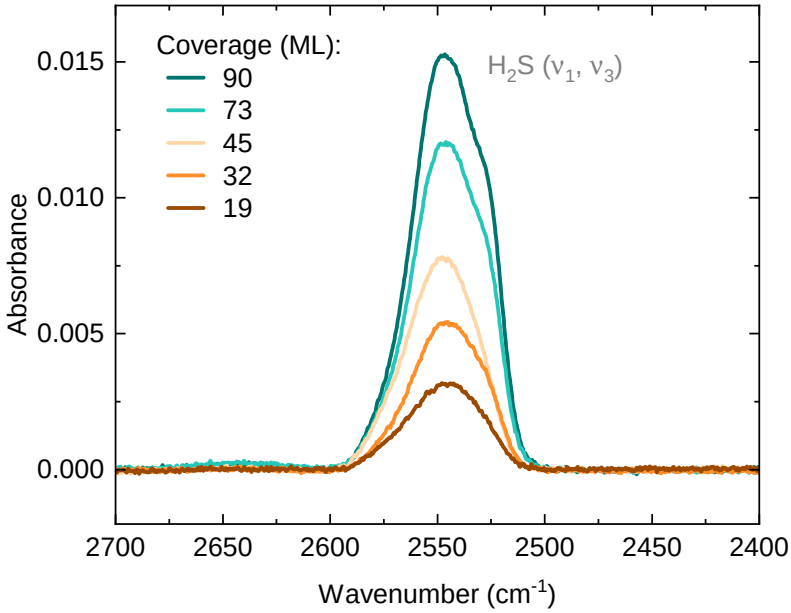

Figure 5.1: Infrared spectra recorded after the deposition of the five different multilayer H_2S ice thicknesses on top of the CsI window. The spectra are centered on the frequency range of the S-H stretching modes of H_2S (ν_1 and ν_3).

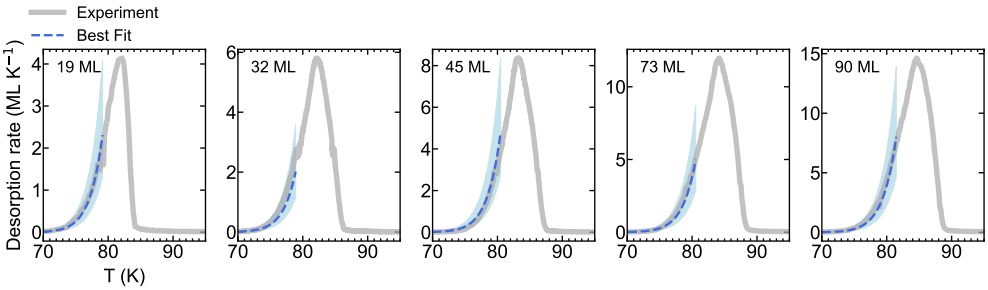

Figure 5.2: TPD curves of the multilayer H_2S ice experiments. The experimental data is shown in gray, while the zeroth-order Polanyi-Wigner models are shown with the dashed blue curve. The shaded blue region indicates the 1σ uncertainty.

As the substrate is warmed up, the morphology of the H_2S ice gradually changes toward more ordered configurations, with amorphous-to-crystalline transitions beginning at temperatures as low at ∼30 K, and nearing completion by ∼60 K (Fathe *et al.* 2006; Mifsud *et al.* 2024). Although the crystallization process appears to be largely finalized by the onset of desorption ($\gtrsim$70 K), the S-H stretching modes of the H_2S ice continue to blueshift as the temperature rises beyond this threshold (see Appendix 5.7.2 and Mifsud *et al.* 2024), indicating an ongoing reorientation of the ice until its complete desorption. This continued reorientation may contribute to deviations from zeroth-order kinetics near the desorption peak, disrupting the exponential trend. Our approach to the choice of temperature reduces the contribution from these confounding factors to the calculation of the preexponential factor.

An alternative, commonly-employed approach is to instead use the peak desorption tem-

perature of the TPD curve. In the case of H_2S, the temperature differences between the two approaches and their overall impact on the desorption parameters are small: the ν_{TST} values derived from the peak desorption T for each coverage (respectively, 82.1, 82.2, 83.0, 84.2, and 84.6 K) deviate by $\lesssim$16% from the values derived by our preferred method, resulting in a less than 3% variation in the corresponding binding energies. Uncertainties in the derived ν_{TST} values stemming from the absolute error of 2 K in the temperature readout are of ∼1%. We emphasize that the H_2S-H_2S binding energy derived in this work corresponds to crystalline H_2S. However, given that the crystallization of H_2S is largely complete by temperatures much lower than its onset of desorption, any thermal desorption of pure H_2S from interstellar ices is expected to occur from its crystalline phase.

The ν_{TST} values derived for each coverage are used to fit their respective TPD curves with the zeroth-order Polanyi-Wigner equation. Following the above reasoning, the fit is performed for the temperature range where the curve maintains an exponential behavior; that is, until the same maximum temperature for which ν_{TST} was calculated. We performed a Monte Carlo analysis using 10,000 independent trials to incorporate and quantify the uncertainties in the ice coverage, absolute substrate temperature, and ν_{TST}. In each trial, temperature, coverage, and ν_{TST} values were randomly sampled from Gaussian distributions defined by their respective uncertainties. A least-squares fit was then applied to the logarithm of the molecule's desorption rate versus the inverse of the temperature, optimizing all five experimental curves simultaneously to derive the binding energy (E_b). This transformation, known as an Arrhenius plot, allows the data to be fitted with a straight line, thus mitigating temperature-dependent fitting biases that can arise when applying Monte Carlo sampling to exponential trends.

This analysis yields a mean best-fit H_2S-H_2S binding energy of $E_b = 3159 \pm 46$ K, shown in the original exponential format by the blue curves in Figure 5.2. The log-transformed Arrhenius fits are shown in Appendix 5.7.3. The uncertainties in E_b are primarily driven by errors in the absolute substrate temperature and in ν_{TST}, as the errors in ice coverage and from the fitting are $\lesssim$1 K. Given that the uncertainties in ν_{TST} due to temperature readout errors are small (∼1%), we adopt the standard deviation from the five experiments (7×10^{14} ML s^{-1}, or ∼4%) as the ν_{TST} error in the fits, which yields uncertainties of $\lesssim$5 K in the binding energy. Consequently, most of the uncertainty in E_b are due to the absolute temperature error. Another approach could be to adopt as uncertainties in ν_{TST} the full range of values derived for the temperatures within the limits encompassed by the fit. However, this also does not affect the results appreciably: while, in this case, ν_{TST} uncertainties correspond to approximately 20%, the resulting mean E_b value remains unchanged, and the error is only increased by 1 K. Additionally, it is also possible to incorporate a temperature-dependent ν_{TST} value into the fit, but this approach produces a poorer fit to the data and was thus not preferred (see Appendix 5.7.4). In some instances, small artifacts are observed at the leading edge, and occasionally symmetrically at the trailing edge of the TPD curves. However, these artifacts have an insignificant impact on the results, with masked fits yielding E_b values that differ by less than 1 K. Table 5.3 summarizes the recommended desorption parameters derived experimentally for the multilayer H_2S ice. The recommended preexponential factor is the mean value between all five thicknesses, with its uncertainty corresponding to their standard deviation: $\nu_{TST} = (1.76 \pm 0.07)\times10^{16}$ ML s^{-1}.

5.3.1.2 H_2S-H_2O

Figure 5.3 shows the TPD curves of the low-coverage H_2S ice grown on top of a cASW substrate. In total, six coverages are depicted: 1.6, 1.2, 0.6, 0.5, 0.3, and 0.2 ML (see Appendix 5.7.1 for details on the submonolayer coverage estimation). The two largest thicknesses, 1.6 and 1.2 ML, show nearly overlapping leading edges that culminate in sharp peaks at ∼77 and ∼76 K, respectively—in accordance with the expected dominating zeroth-order desorption behavior. In contrast, the submonolayer coverages display a markedly different

Table 5.3: Summary of the H_2S desorption parameters derived experimentally in this work

Regime	Substrate	n	Coverage (ML)	E_b (K)	ν_{TST} (ML^{1-n} s^{-1})
H_2S-H_2S	CsI window	0	19−90	3159 ± 46	$(1.76 \pm 0.07)\times10^{16}$
H_2S-H_2O	cASW	1	0.6	3355 [179] [a]	$(1.69 \pm 0.04)\times10^{16}$
H_2S-H_2O	cASW	1	0.5	3368 [172] [a]	$(1.72 \pm 0.04)\times10^{16}$
H_2S-H_2O	cASW	1	0.3	3401 [169] [a]	$(1.83 \pm 0.05)\times10^{16}$
H_2S-H_2O	cASW	1	0.2	3443 [191] [a]	$(1.85 \pm 0.05)\times10^{16}$

Notes. [(a)] Square brackets denote the FWHMs of the binding energy distributions.

profile, with misaligned leading edges and peak desorption temperatures that increase slightly with decreasing coverages ($T_{peak} \sim 79.3$, 79.6, 81.1, and 81.3 K for 0.6, 0.5, 0.3, and 0.2 ML). This behavior is consistent with pure first-order desorption, and therefore the 0.6−0.2 ML coverages are used to derive the H_2S-H_2O binding energy (dominated by H_2S interactions with water).

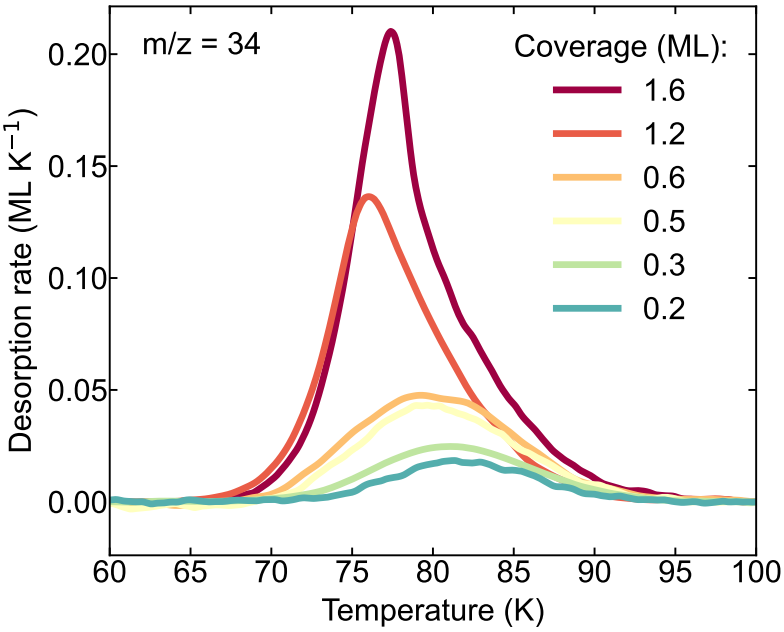

Figure 5.3: TPD curves of the low-coverage H_2S ice experiments deposited on top of a cASW substrate. The transition from zeroth-order to pure first-order sublimation behavior is seen for coverages <1.2 ML. The experimental data is smoothed for clarity.

In the case of the submonolayer TPD curves, unlike the multilayer curves, the entire desorption profile is fitted to find E_b. As a result, the peak desorption temperature of the curve is encompassed by the model, and thus we calculate ν_{TST} at the peak value for each coverage—which reflects the transition state of the largest parcel of desorbed H_2S molecules. Also differently from the multilayer regime, the TPD curves of the submonolayer H_2S ice cannot

be described by a single binding energy (see Appendix 5.7.5 for an example of an attempted fit). This is a direct consequence of the non-homogeneous nature of the cASW substrate, which generates multiple binding sites that result in a range of H_2S-H_2O desorption energies. To account for that, we fit a linear combination of first-order Polanyi-Wigner equations (eq. 5.3) to the curves, with statistical weights normalized to the initial ice coverages for each experiment. This allows us to determine the relative population of each binding site. The same approach has been used in the past to derive submonolayer binding energies of hypervolatiles such as N_2 and CO, as well as less volatile molecules such as 2-C and 3-C hydrocarbons and methanol, on varying substrates (from water ice to graphite; Doronin *et al.* 2015; Fayolle *et al.* 2016; Behmard *et al.* 2019). Since the preexponential factor is calculated using equations 5.4, 5.5, and 5.6, it is treated as a fixed parameter when fitting the curves with a linear combination of Polanyi-Wigner equations. Our sampled desorption energies range from 2000 to 4500 K in steps of 90 K, chosen to balance fit resolution and degeneracies associated with smaller bin sizes. Figure 5.4 shows the resulting fits to the submonolayer TPD curves and their corresponding binding energy distributions, plotted as fractional coverages as a function of the energy.

The population histograms can be approximated by a normal distribution and are thus fitted by a Gaussian curve to allow for more straightforward interpretation (red dashed line in the right panels in Figure 5.4). The mean binding energy and FWHM values for each coverage are listed in Table 5.3 and can be regarded as representative desorption energies for each ice thickness. The corresponding ν_{TST} values used in the fits are also listed, with their uncertainties stemming from the absolute error in the substrate temperature. Among the four coverages, the average binding energy and preexponential factor are $E_b = 3392 \pm 56$ K and $\nu_{\mathrm{TST}} = (1.7 \pm 0.1) \times 10^{16}$ s^{-1}. The uncertainty of E_b encompasses the relative error due to the step size in the binding energy sampling and the standard deviation among the four coverages, while for ν_{TST} it is taken solely from its standard deviation.

5.3.1.3 Binding energies vs coverage

In Figure 5.5, we show a comparison of all H_2S binding energies derived in this work as a function of coverage. The multilayer binding energy ($E_b \sim 3159$ K) is slightly lower than the submonolayer values, with a difference of ∼7% w.r.t the average submonolayer E_b (∼ 3392 K). This small difference suggests that the H_2S-H_2S interactions are only moderately weaker than the H_2S-H_2O counterparts. This is rather expected: both H_2S and H_2O interact via hydrogen bonding networks—known as one of the strongest intermolecular forces—where hydrogen atoms are covalently bonded to an electronegative atom. Since sulfur is larger than oxygen, it is less electronegative, and therefore the H-bonding networks are weaker for H_2S than for H_2O. Indeed, the fact that pure first-order desorption could be achieved at coverages of ∼0.6 ML (as evinced by the profile of the TPD curves in Figure 5.3, see section 5.3.1.2) suggests that wetting of the H_2S on the cASW surface proceeds relatively uniformly, as opposed to having a tendency to form H_2S islands (for comparison, Bergner *et al.* 2022 found that a dose of 0.04 ML was required to achieve the first-order desorption regime for HCN on cASW). This is in line with a (modest) preference of H_2S to interact with H_2O.

In the submonolayer regime, the mean H_2S-H_2O binding energy increases with decreasing ice coverage, in line with other laboratory measurements for various adsorbate-substrate combinations (e.g., Noble *et al.* 2012; Fayolle *et al.* 2016; He *et al.* 2016a; Nguyen *et al.* 2018; Behmard *et al.* 2019). This generalized phenomenon can be explained by two effects: 1. lateral interactions influencing the binding energy of the adsorbates, or 2. a preference of the adsorbates to occupy deeper binding sites (caused by their diffusion from shallower sites)—with the most likely explanation being a combination of the two. The weaker H_2S-H_2S interactions relative to H_2S-H_2O may manifest as a slight decrease in binding energy caused by lateral H_2S interactions compared to isolated H_2S adsorbates fully interacting with H_2O, in support of explanation 1. Complementarily, the alignment of the trailing edges in the

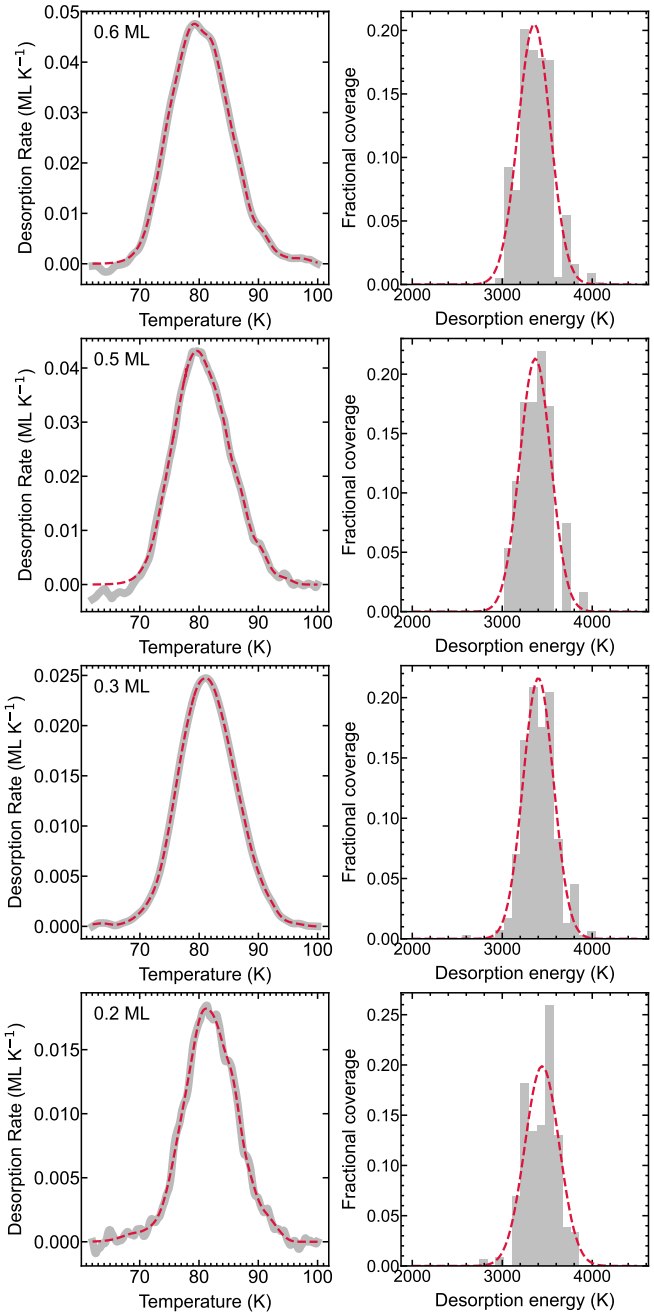

Figure 5.4: Results of the fits to the submonolayer H_2S ice data. Each row corresponds to a different H_2S ice thickness: ∼0.6, ∼0.5, ∼0.3, and ∼0.2 ML (from top to bottom). Left panels show the TPD curves with the experimental data in gray and the fits with a linear combination of first-order Polanyi-Wigner equations in red. Right panels show the corresponding binding energy distribution: normalized fractional coverages are shown as a functional of the binding energy (gray histogram), superimposed by a Gaussian fit to the distribution (red dashed line).

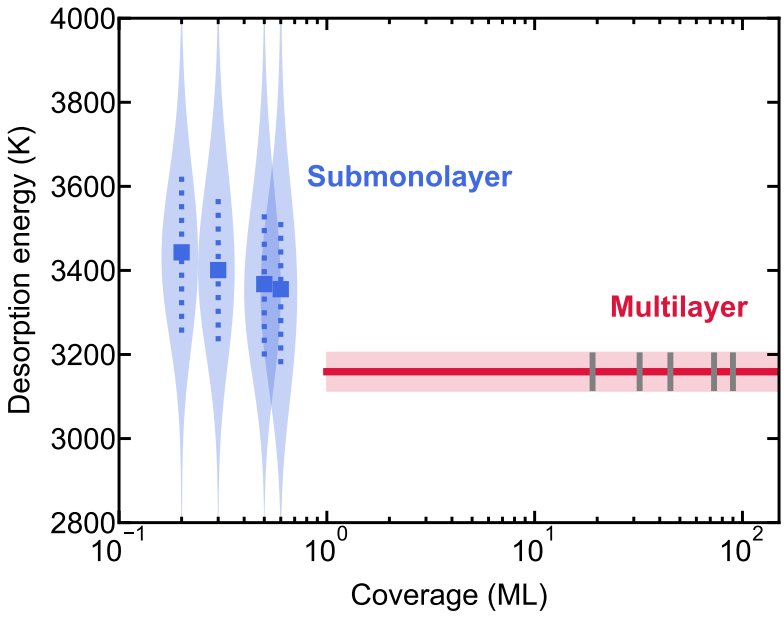

Figure 5.5: Desorption energies derived experimentally in this work as a function of H_2S ice thickness. For the submonolayer regime, the binding energies are represented by blue violin plots, where the square markers indicates the mean binding energies, and the vertical dotted lines show the FWHMs of the Gaussian fits to the binding energy distributions for each coverage. The contour of each violin plot reflects the full range of the sampled binding energy distribution, with its thickness normalized according to the statistical weights (or fractional coverages) of each E_b value. The multilayer binding energy is depicted as a red solid line with its uncertainty shown by the light-red shadowed area. The five different ice coverages used to derive the multilayer E_b are shown as gray vertical lines.

submonolayer experiments suggests that the deeper binding sites are similarly occupied for all explored thicknesses, reinforcing explanation 2.

To the best of our knowledge, this is the first study to experimentally determine binding energies for H_2S ice analogues. Nonetheless, estimations based on laboratory data have been proposed in the past. Minissale *et al.* (2022) recommend a value of E_b = 3426 K for H_2S on a cASW substrate based on the peak desorption temperature of H_2S and the associated ν obtained using the TST formalism—in good agreement with our measurements. In contrast, the E_b value of 2296±9 K estimated by Penteado *et al.* (2017), based on the relative peak desorption temperature of H_2S with respect to H_2O and the binding energy of the latter, differs significantly from our measurements. Computational efforts have also been made to estimate the binding energies of H_2S. In general, computed E_b distributions for H_2S on water substrates range between $\sim 2000 - 3600$ K (Wakelam *et al.* 2017; Das *et al.* 2018; Ferrero *et al.* 2020; Piacentino & Öberg 2022), but some studies predict much lower ranges, with upper limits closer to 2000 K (Oba *et al.* 2018; Bariosco *et al.* 2024). The experimental values reported here for $H_2S{-}H_2O$ (and $H_2S{-}H_2S$) are generally not well reproduced by the computations, often falling within their upper bounds or, in some cases, being entirely underpredicted. This discrepancy is likely due to the limitations in the computational methods to incorporate diffusion as part of their binding energy calculations, which can lead to systematic underestimations by failing to account for the tendency of adsorbates to settle into deeper binding sites prior to sublimating. In an astrophysical context, icy mantles shrouding

dust grains are gradually heated by protostellar radiation, in which case adsorbates in shallow sites become free to diffuse throughout the ice and find deeper binding sites before eventually sublimating. The binding energies derived from TPD experiments are therefore expected to better reproduce the conditions in space.

5.3.2 Entrapment in H_2O

The entrapment behavior of H_2S in water-dominated ice was investigated by TPD experiments of H_2O:H_2S ice mixtures with four different ratios (5.1:1, 7.5:1, 9.3:1, and 17:1, determined from the final IR spectra measured after deposition) and constant total ice thicknesses ($\sim$40 ML). These mixing conditions are chosen to ensure that H_2S is mostly surrounded by H_2O molecules while still allowing for measurements with good signal-to-noise ratios, particularly for the more water-dominated cases. Additionally, a control experiment consisting of $^{13}CO_2$ mixed in H_2O ice with a ratio of H_2O:$^{13}CO_2$=14:1 was also performed with the goal of testing the potential role of intermolecular interactions on the entrapment efficiencies. Both H_2S and CO_2 have similar volatilities, with desorption temperatures typically falling in similar ranges for the same pressure and substrate conditions. However, CO_2 is an apolar molecule and its intermolecular interactions with H_2O are markedly different from those of H_2S. The resulting TPD curves of the H_2O:H_2S = 9.3:1 experiment, as well as the control H_2O:$^{13}CO_2$ = 14:1 experiment, are shown in the upper and lower panels of Figure 5.6, respectively.

Two desorption features are observed for H_2S ice mixed in H_2O: a monolayer desorption peak at $\sim$84 K, and a molecular volcano feature at $\sim$150 K. The former is consistent with H_2S desorption characterized by the H_2S-H_2O binding energy (see Appendix 5.7.6), and includes contributions from H_2S adsorbates on the uppermost ice layer, as well as H_2S molecules occupying channels within the H_2O matrix with access to the surface. The molecular volcano is the strongest desorption peak, and corresponds to H_2S being released from the H_2O ice matrix as the ice crystallizes and cracks, creating new channels to the surface. In the case of $^{13}CO_2$, a third desorption regime is observed ranging from $\sim 90-140$ K. Following its monolayer desorption feature at $\sim$80 K, the TPD curve does not return to zero desorption rate, but instead shows a relatively steady desorption of $^{13}CO_2$ until the molecular volcano feature at $\sim$150 K—after which it appears to be completely sublimated. This continuous desorption between the two main features might be related to the diffusion of $^{13}CO_2$ through the H_2O ice.

Table 5.4 lists and Figure 5.7 depicts the entrapment efficiencies of H_2S and $^{13}CO_2$ measured from our mixed-ice experiments (see section 5.2.3 for details on how these are determined). The uncertainties are dominated by experimental variability and are thus taken as 10% of the entrapment efficiency, based on the estimations derived by Simon *et al.* (2023) with the same experimental setup for H_2O:hypervolatile mixtures with ratios 3:1. In comparison, the error due to stochastic instrumental noise amounts to $\lesssim$2%. Overall, H_2S experiences very efficient entrapment in the H_2O-ice matrix, with $\sim 76-85$% of the H_2S unable to escape to the gas phase until H_2O undergoes significant structural changes. This efficient entrapment of H_2S has been alluded to in the past by Jiménez-Escobar & Muñoz Caro (2011a) based on experiments using H_2O:H_2S ice mixtures with roughly 10% H_2S concentrations. Larger water abundances relative to H_2S result in higher entrapment efficiencies, consistent with the behavior observed for many other species mixed in H_2O and CO_2-dominated ices (Fayolle *et al.* 2011; Martín-Doménech *et al.* 2014; Simon *et al.* 2019, 2023; Kruczkiewicz *et al.* 2024; Pesciotta *et al.* 2024). Fayolle *et al.* (2011) propose two explanations for this phenomenon: 1. there is a reduction in porous channels connected to the surface for higher dilutions of the volatile; and/or 2. higher volatile concentrations increase its diffusion lengths. The two highest dilutions (H_2O:H_2S $\sim$9:1 and 17:1) yield analogous efficiencies within their uncertainties, signaling that the trapping capacity of H_2S in the H_2O ice saturates at $\sim$85% for our deposition conditions and a total ice thickness of $\sim$40 ML. Similarly, Pesciotta *et al.* (2024) recently reported a leveling-off of the entrapment efficiencies of CO in both H_2O and

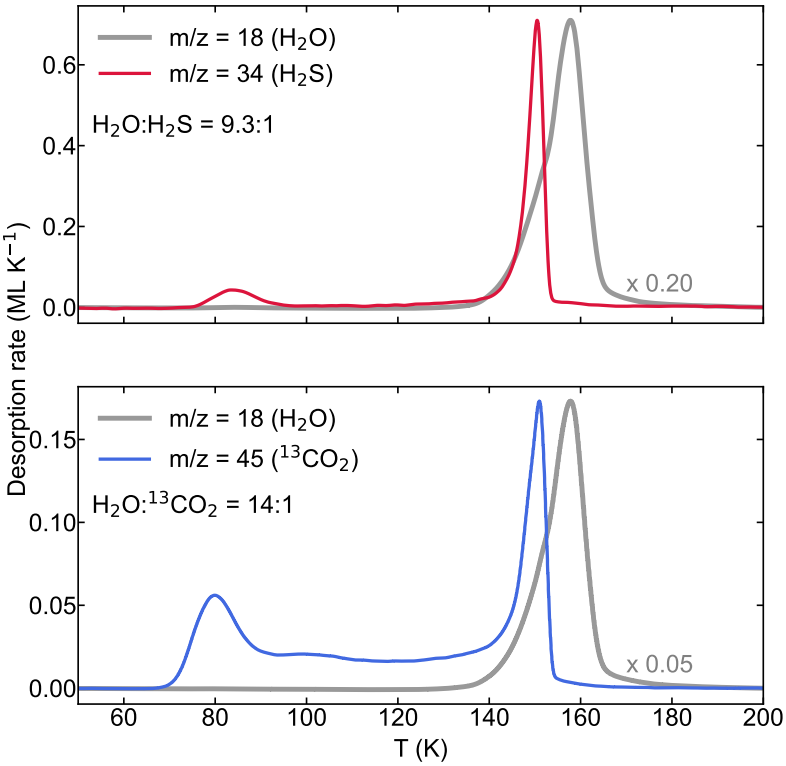

Figure 5.6: TPD curves of two mixed-ice experiments, H_2O:H_2S = 9.3:1 (top) and H_2O:$^{13}CO_2$ = 14:1 (bottom). The desorption data of H_2O, H_2S, and $^{13}CO_2$ are shown in gray (m/z = 18, $[H_2O]^+$), red (m/z = 34, $[H_2S]^+$), and blue (m/z = 45, $[^{13}CO_2]^+$), respectively. Two desorption regimes are seen for H_2S: a submonolayer H_2S-H_2O desorption feature and a molecular volcano desorption peak. For $^{13}CO_2$, a third regime is observed between its submonolayer and volcano peaks, indicating constant sublimation within that temperature range.

CO_2 dominated binary ice mixtures starting at concentrations of $\lesssim$1:10 volatile:matrix. We emphasize, however, that the CO entrapment saturation measured in their work occurred at significantly lower efficiencies than the saturation point for H_2S in H_2O measured here (they find ∼69% and ∼61% for CO_2 and H_2O matrices, respectively, in 1:15 CO:matrix ratios and ice thicknesses $\gtrsim$50 ML).

In comparison to H_2S, $^{13}CO_2$ is significantly less entrapped in the H_2O ice, with an efficiency of ∼ 52% for a H_2O:$^{13}CO_2$ ratio of ∼14:1. This stark difference between two similarly volatile molecules might be explained by the nature of their interactions with the water matrix. For $^{13}CO_2$, the oxygen atoms may serve as hydrogen bond acceptors; however, their very low partial negative charges result in exceptionally weak hydrogen bonds (Zukowski *et al.* 2017). Interactions between $^{13}CO_2$ and H_2O are thus primarily governed by weaker van der Waals forces. In contrast, the hydrogen bonds between H_2S and H_2O, while not as strong as H_2O-H_2O counterparts (Craw & Bacskay 1992), still offer significant energetic stabilization. This is reflected in the mean H_2S-H_2O binding energy measured here at 3392±56 K, which surpasses the CO_2-H_2O binding energies measured in the literature by

Table 5.4: Summary of the entrapment efficiencies derived experimentally in this work.

Mixture	Ratio	Entrapment efficiency (%)
H_2O:H_2S	5.1:1	76±8
H_2O:H_2S	7.5:1	80±8
H_2O:H_2S	9.3:1	86±9
H_2O:H_2S	17:1	85±9
H_2O:$^{13}CO_2$	14:1	52±5

Notes. All experiments kept a constant total ice thickness of ∼40 ML.

∼50−60%[3]. In fact, both Noble *et al.* (2012) and Edridge *et al.* (2013) reported CO_2−CO_2 binding energies to be higher than the mean value for those of CO_2−H_2O, in clear contrast with the behavior observed here for H_2S and water. The difference in the interaction energetics between the two systems (H_2O:$^{13}CO_2$ vs H_2O:H_2S) may result in H_2S diffusing less readily through H_2O ice compared to $^{13}CO_2$, leading to more efficient trapping of H_2S. Indeed, the steady desorption of $^{13}CO_2$ between its monolayer and volcano peaks may suggest that it is more mobile than H_2S, for which this behavior is minimal. Specifically, this temperature range accounts for $\lesssim 5\%$ of the integrated QMS signal in all H_2S experiments, and corresponds to only $\sim 2\%$ in the H_2O:H_2S = 9.3:1 mixture, compared to $\sim 21\%$ for $^{13}CO_2$ in a higher dilution.

In addition to intermolecular interactions, the mass and size of the molecule may also influence its diffusion and entrapment. Based on their molecular masses and kinetic diameters, $^{13}CO_2$ is ∼30% heavier and ∼9% smaller than H_2S ($m_{^{13}CO_2} \sim 45$ amu vs $m_{H_2S} \sim 34$ amu; $d_{^{12}CO_2} \sim 3.3$ vs $d_{H_2S} \sim 3.6$, Matteucci *et al.* 2006; Ismail *et al.* 2015). Considering the mass effect alone, the attempt frequency for diffusion of $^{13}CO_2$ would be smaller than that of H_2S, resulting in the former diffusing slower (see, e.g., Cuppen *et al.* 2017) and consequently being more efficiently trapped. The fact that the inverse is observed in our experiments signals that the mass effect is overpowered by other factors favoring the entrapment of H_2S. In contrast, the size difference could result in H_2S molecules being more efficiently trapped if the mean pore size is smaller than the kinetic diameter of H_2S, but larger than that of $^{13}CO_2$. This size mismatch may create a geometrical limitation, with the pores acting similarly to a net that restricts diffusion. For instance, gas permeance through microporous silica membranes (pore size between $3.8-5.5$) has been shown to decrease steeply with the species' kinetic diameter, with the permeance of N_2 ($d \sim 3.6$, similar to H_2S; Ismail *et al.* 2015) being roughly one order of magnitude lower than that of CO_2 (De Vos & Verweij 1998). ASW ices are typically found to be microporous (pore width ≤ 20), with no lower limits estimation for the pore sizes and little to no incidence of mesopores (Mayer & Pletzer 1986; Raut *et al.* 2007; Cazaux *et al.* 2015; Carmack *et al.* 2023). This is particularly true for ices grown through collimated deposition—the technique employed in this work. The possibility of a pore effect therefore cannot be ruled out. Pore effects could also play a role in the constant sublimation regime of CO_2, observed between its monolayer and volcano features. The same behavior is seen for $^{12}CO_2$:H_2O ice mixtures in Kruczkiewicz *et al.* (2024), though they note that this is not observed for other, more volatile species (such as Ar and CO) trapped in H_2O-dominated binary ices. Since both Ar and CO have larger kinetic diameters than CO_2 ($d_{Ar} \sim 3.4$ and $d_{CO} \sim 3.8$; Breck 1973; Matteucci *et al.* 2006), the fact that they do not display the constant

[3]Noble *et al.* (2012) and Edridge *et al.* (2013) measured the mean monolayer CO_2 binding energy on ASW to be ∼2247 K and ∼2100 K, respectively. The former was measured on a nonporous ASW substrate, while the latter was measured on porous ASW.

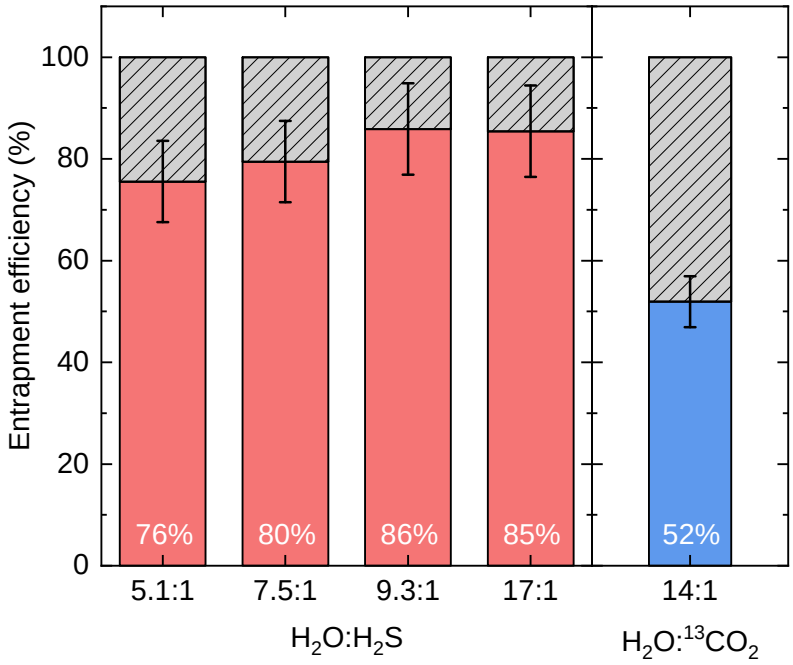

Figure 5.7: Efficiencies with which H_2S (red) and $^{13}CO_2$ (blue) are trapped in water-rich binary ice mixtures as derived from our experiments (see also Table 5.4).

sublimation regime in the experiments by Kruczkiewicz *et al.* (2024) does not preclude this possibility. Dedicated experimental investigations are necessary to fully constrain the effect of the species' size and intermolecular interactions to entrapment. Nonetheless, the overall result is that H_2S is very efficiently entrapped in H_2O ice, more so than other similarly volatile molecules, which has significant implications to its gas vs ice distribution in planet-forming regions.

5.4 Astrophysical implications

The binding energies derived experimentally in this study are used to estimate the locations of the H_2S sublimation fronts in the midplane of a representative protoplanetary disk. First, we calculate the desorption temperatures of H_2S for its two binding energies ($H_2S{-}H_2S$ and $H_2S{-}H_2O$) following the formalism by Hollenbach *et al.* (2009), in which the desorption temperature is found by equating the flux of molecules adsorbing on the grain surface to the flux of molecules desorbing from it:

$$T_i \sim (E_{b,i}/k) \left[\ln \left(\frac{4 N_i f_i \nu}{n_i v_i} \right) \right]^{-1}, \tag{5.7}$$

where T_i is the sublimation temperature of species i, $E_{b,i}$ is its binding energy, N_i is the number of adsorption sites (assumed to be $\sim 10^{15}$ cm^{-2}), f_i is the fraction of such sites occupied by species i, and ν_i is its vibrational frequency in the surface potential well (i.e., the preexponential factor in equation 5.3). In the denominator, n_i is the number density of species i in the gas phase, and v_i is its thermal speed. We estimate f_i based on the cometary abundance of H_2S relative to water, $H_2S/H_2O = 1.10 \pm 0.05\%$, as measured by the

Rosetta mission on the coma of comet 67P (Calmonte *et al.* 2016); and assuming a cometary composition of $\sim 80\%$ water (e.g., Delsemme 1991). The number density n_i is estimated by multiplying the cometary H_2S/H_2O by the water abundance with respect to H and the number density of hydrogen nuclei in a disk midplane (taken as $H_2O/H \sim 10^{-4}$, e.g., Drozdovskaya *et al.* 2015; Boogert *et al.* 2015; and $n_H \sim 10^{10}$ cm $^{-3}$, e.g., Walsh *et al.* 2014). This yields sublimation temperatures for $H_2S{-}H_2S$ and $H_2S{-}H_2O$ of ~64 K and ~69 K, respectively. For the latter, the mean $H_2S{-}H_2O$ binding energy value was used ($E_b \sim 3392$ K). We note that the desorption temperatures in the disk model differ from those in the laboratory due to variations in physical conditions between the two environments.

To derive the locations of the sublimation fronts, we assume a representative disk midplane radial temperature profile:

$$T = 200 \times r^{-0.62}, \tag{5.8}$$

where r is the radial distance in a.u. This corresponds to the median midplane temperature distribution found for a sample of 24 T-Tauri disks (Andrews & Williams 2007). The resulting sublimation front locations are shown in Figure 5.8.

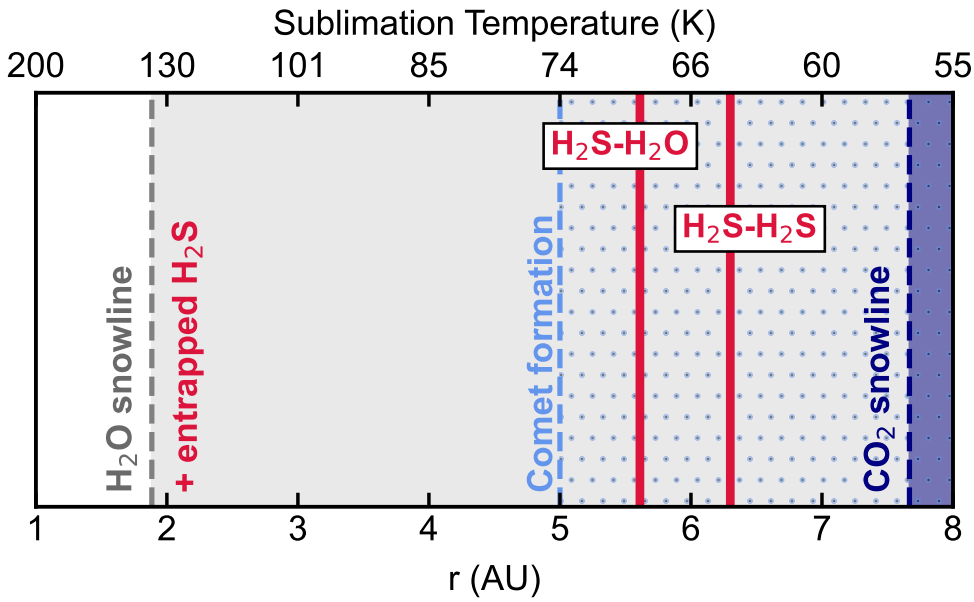

Figure 5.8: Sublimation front locations for the $H_2S{-}H_2S$ and $H_2S{-}H_2O$ binding energies estimated for a representative T-Tauri disk midplane. Most of the H_2S will remain entrapped in the ice past its sublimation front radii, and will only be released to the gas phase close to the water snowline. The CO_2 snowline location is also shown for comparison. It was estimated based on the mean binding energy derived by Noble *et al.* (2012) for (sub)monolayer CO_2 ice on a nonporous ASW surface and their adopted preexponential factor of 10^{12} s^{-1}, while assuming ice abundances $N(CO_2)/N(H_2O)$~0.28 (median value observed in low-mass young stellar objects; Boogert *et al.* 2015).

The sublimation fronts for the $H_2S{-}H_2S$ and $H_2S{-}H_2O$ binding energies occur at ~6.3 au and ~5.6 au, respectively. The former corresponds to pure H_2S ice desorption, while the latter is relevant for H_2S desorbing from a H_2O-rich surface. In the case of H_2S entrapped in water ice, its sublimation will be delayed to much closer to the water snowline at ~1.9 au (assuming $E_{b,H_2O} \sim 5600$ K, Wakelam *et al.* 2017; and a typical $\nu \sim 10^{13}$ s^{-1}). The precise location of this sublimation front will depend on the water crystallization kinetics, but will

generally occur at slightly lower temperatures than H_2O desorption, placing it just beyond the H_2O snowline.

The deuterium fractionation of gaseous H_2S observed towards Class 0 protostars suggests that it is formed in ices during early prestellar cloud timescales, before the onset of the catastrophic CO freeze-out (Ceccarelli *et al.* 2014). Most of the water ice is also formed during similarly early timescales, resulting in H_2S likely inhabiting a H_2O-rich ice environment—the so-called polar ice layer. The sublimation behavior of H_2S will therefore be likely dominated by its entrapment within H_2O ice, given its high efficiency as measured in this work ($\sim$85% for H_2S concentrations of $\sim$5$-$10% in H_2O). In more representative interstellar scenarios, the bulk H_2S concentration in H_2O ice is expected to be considerably smaller ($\lesssim$1% based on observationally-constrained H_2S ice upper limits), and ice thicknesses larger ($\gtrsim$0.01 μm; Dartois *et al.* 2018) than our experimental conditions. Like for higher dilutions, entrapment efficiencies have been shown to increase with ice thickness (Fayolle *et al.* 2011; Simon *et al.* 2019; Bergner *et al.* 2022; Simon *et al.* 2023; Kruczkiewicz *et al.* 2024), though this dependency might break down for thicknesses $\gtrsim$50 ML (Pesciotta *et al.* 2024). Moreover, the deposition temperatures used in our entrapment experiments generate porous amorphous water ice matrices, whereas more representative cASW might trap volatiles more efficiently than porous counterparts (Kruczkiewicz *et al.* 2024).[4] These three factors (mixing ratios, thicknesses, and water ice morphology) thus point to real H_2S entrapment efficiencies being higher than the values measured here, further highlighting the shift in the H_2S sublimation front closer to the water snowline. At the same time, differences between the heating rates used in the laboratory and those occurring in astrophysical timescales could result in an overestimation of the measured entrapment efficiencies (Cuppen *et al.* 2017). Moreover, since sulfur atoms are heavier and less abundant than oxygen, the bulk of the H_2S ice has been predicted to form at slightly later timescales (by $\sim$1.4 A_V) than H_2O (Goicoechea *et al.* 2021). This differential formation could result in a concentration gradient for H_2S within the polar ice layer, meaning that a fraction of H_2S could exists in higher local concentrations than the estimated $\lesssim$1%. In any case, the very efficient entrapment of H_2S in water, with measured efficiencies of $\gtrsim$75% for H_2S concentrations even as high as $\sim$20%, means that even in these scenarios, a significant portion of H_2S will remain entrapped in water.

Some ice species, such as CO_2 and potentially HCN, exhibit a segregation behavior upon heating, where diffusion leads to the formation of pockets of pure ice instead of a homogeneous mixture (e.g., Öberg *et al.* 2009a; Boogert *et al.* 2015; Bergner *et al.* 2022). For H_2S, segregation appears to be less energetically favorable than for the archetypal case of CO_2. Unlike CO_2, the H_2S-H_2O binding energies exceed that of H_2S-H_2S, and H_2S appears to wet the cASW surface effectively. However, the significantly stronger stabilization among H_2O molecules themselves compared to H_2S-H_2O interactions ($E_b(H_2O-H_2O) \sim 5600$ K; Wakelam *et al.* 2017) may still drive some degree of segregation, as a system with separate water-rich and H_2S-rich pockets can be energetically more favorable than a fully mixed one. Similar energetic considerations are required in the kinetic Monte Carlo simulations performed by Öberg *et al.* (2009a) to reproduce the segregation behavior they observed experimentally for CO_2:H_2O mixed ices. [5] Consequently, in an astrophysical context, a fraction of H_2S within channels with access to the surface might desorb at the sublimation fronts defined by

[4]Previously, Burke & Brown (2010) suggested that more compact ASW should result in lower entrapment efficiencies due to a reduction in available trapping sites. This interpretation was based on earlier experiments by Bar-Nun *et al.* (1988), which observed lower entrapment efficiencies of hypervolatiles in binary mixtures with water ice as the deposition temperature increased. However, this decline is more likely dominated by the reduced surface residence time of hypervolatiles at higher deposition temperatures (Zhou *et al.* 2024), rather than due to the water ice morphology. Recently, Kruczkiewicz *et al.* (2024) deposited cASW ices at 10 K using well-collimated beams, and found that trapping capacities were actually higher for the compact ice structure.

[5]Öberg *et al.* (2009a) find that segregation in CO_2:H_2O ice mixtures is not precluded by CO_2-CO_2 binding energies being lower than those of CO_2-H_2O. Rather, it might occur when a CO_2 molecule from a water-dominated environment is swapped with a H_2O molecule from a CO_2-dominated en-

H_2S-H_2S and H_2S-H_2O interactions, depending on the extent of segregation.

Nonetheless, the primary sublimation front of H_2S is driven by its entrapment. This effectively shifts the H_2S sublimation front closer to the protostar by nearly threefold, fully retaining H_2S in the ice throughout and beyond the comet-formation zone (> 5 au; Mandt *et al.* 2015), and across the region where other H_2O-rich bodies, such as icy asteroids, are formed. Consequently, H_2S may be incorporated into planetesimal cores formed beyond the water snowline ($\sim$1.9 au), which in turn may deliver it to terrestrial planets. In fact, Rosetta measurements of the H_2S/H_2O ratios in the coma of comet 67P remained remarkably constant over several months, strongly suggesting that H_2S desorbs from the comet nucleus along with H_2O (Calmonte *et al.* 2016). This supports the hypothesis that H_2S is incorporated into cometary cores mixed with H_2O, where it remains preserved beyond its sublimation temperature, until water ice desorption.

Additionally, solid-state H_2S can react with NH_3 to form the ammonium salt $NH_4^+SH^-$—a likely major carrier of both nitrogen and sulfur in comets (Altwegg *et al.* 2022; Slavicinska *et al.* 2025). Upon sublimation, this salt decomposes back into its neutral reactants, releasing H_2S (and NH_3) into the gas phase. The desorption temperature of the salt is nearly identical to that of water, meaning that the gaseous H_2S released from the decomposition of the salt will have a sublimation front similar to that of neutral H_2S entrapped in H_2O. Distinguishing the contribution from the neutral H_2S and the salt to the gas-phase distribution of H_2S in disks presents a challenge, but it could be an interesting avenue for future exploration. We emphasize that the neutral H_2S component within interstellar ices is likely significant, as the $NH_4^+SH^-$ salt detected by the Rosetta mission is found in the comet's grains, while the ice predominantly contains H_2S in its neutral form (Altwegg *et al.* 2022).

5.5 Conclusions

In this work, we provide a comprehensive characterization of the thermal sublimation dynamics of H_2S ice. We investigate its binding energies both dominated by interactions with other H_2S molecules (H_2S-H_2S) and with H_2O molecules (H_2S-H_2O), as well as the efficiency with which it is entrapped in water-rich ices. This information is used to estimate the different snowline positions of H_2S in the midplane of a representative T-Tauri protoplanetary disk. Our main findings are as follows:

1. We derive $E_b = 3159 \pm 46$ K for the H_2S-H_2S binding energy, with a mean preexponential factor of $\nu = (1.76 \pm 0.07) \times 10^{16}$ ML s^{-1}.
2. For H_2S-H_2O, we find four sets of desorption parameters for four different H_2S coverages (0.6, 0.5, 0.3, and 0.2 ML). The mean binding energy and preexponential factor are $E_b = 3392 \pm 56$ K and $\nu = (1.7 \pm 0.1) \times 10^{16}$ s^{-1}.
3. Theoretical H_2S binding energies generally underpredict the experimental values derived in this work. We propose this mismatch is due to a limitation in the computations to account for adsorbate diffusion causing a preference for occupying deeper surface biding sites. In interstellar and protoplanetary conditions, diffusion plays an important role in a molecule's sublimation dynamics, and therefore our experimentally-derived binding energies are expected to be more representative values.
4. H_2S is very efficiently entrapped in H_2O ice, with efficiencies of $\sim 75-85\%$ for H_2O:H_2S mixing ratios of 1:$\sim 5-17$ (more diluted cases yielding more efficient entrapment). In comparison, $^{13}CO_2$ is much less efficiently entrapped, with an efficiency of $\sim$52% for a H_2O:$^{13}CO_2$ ratio of 1:14. We suggest this might be due to the hydrogen bonding networks between H_2S and H_2O, which are stronger intermolecular interactions that

vironment. This process only requires that $0.5\times E_b(H_2O-H_2O)+0.5\times E_b(CO_2-CO_2)$ is greater than $E_b(H_2O-CO_2)$.

the induced dipoles between $^{13}CO_2$ and H_2O. Pore effects could also play a role in entrapping H_2S more efficiently than $^{13}CO_2$.

5. Our measured H_2S-H_2S and H_2S-H_2O binding energies yield H_2S sublimation temperatures at ∼64 K and ∼69 K, respectively. This corresponds to a radial distance of ∼6.3 au and ∼5.6 au in the midplane of a representative T-Tauri disk.

6. The vast majority of H_2S will remain entrapped in the ice until water crystallizes at radii close to the H_2O snowline, shifting its sublimation front inward by nearly a factor of three. As a result, most of the H_2S will remain in ices throughout the region where water-rich icy planetesimals form.

5.6 Acknowledgements

J.C.S. acknowledges support from the Danish National Research Foundation through the Center of Excellence "InterCat" (Grant agreement no.: DNRF150) and the Leiden University Fund / Fonds Van Trigt (Grant reference no.: W232310-1-055). K.I.Ö. acknowledges an award from the Simons Foundation (#321183FY19).

5.7 Appendix

5.7.1 Submonolayer coverage estimation

The submonolayer H_2S coverages were estimated based on a QMS-to-column density scaling factor, f, derived from the multilayer H_2S experiments. Figure 5.9 shows the correlation between the H_2S ice column density obtained from the integrated absorbance of its S-H stretching feature (see Equation 5.2) and the integrated signal of the H_2S desorption feature as measured by the QMS for m/z = 34.

A linear fit to the plot gives the conversion factor $f = (3.2 \pm 0.4) \times 10^{26}$ A^{-1} K^{-1}. In the low coverage experiments, where H_2S was deposited on top of cASW, the H_2S ices with approximately 1.6 ML and 1.2 ML (determined from their infrared absorbance bands) produced S-H stretching features detectable above our instrumental noise. By comparing the measured and predicted H_2S coverages in these experiments, we estimate that the submonolayer coverages might be underpredicted by up to a factor of 2 using our scaling method. However, this discrepancy does not impact our analysis, as the higher coverages (by a factor of two) yield binding energy distributions with mean E_b values differing by less than 2 K from those derived for the predicted coverages—well within their FWHMs.

5.7.2 Pure H_2S ice infrared features vs temperature

Figure 5.10 shows the IR spectra recorded during the TPD experiment of a multilayer H_2S ice with an initial coverage of 73 ML. The splitting between its symmetric (ν_1) and antisymmetric (ν_3) S-H stretching modes signals that ice crystallization starts to occur at temperatures as low as ∼30 K. By ∼65 K, the transition to phase III crystalline H_2S is nearly complete. However, from ∼65 K up to the point of complete desorption, a continuous blueshift in the S-H stretching features is observed, suggesting ongoing structural reorganization within the ice. While higher-energy crystalline phases of H_2S exist (phase II transitioning at ∼100 K and phase I transitioning at ∼125 K, see Fathe *et al.* 2006 and references therein), these transitions are observed under ambient pressure and occur above the sublimation temperature of H_2S in UHV conditions. They are therefore not relevant to our experiments.

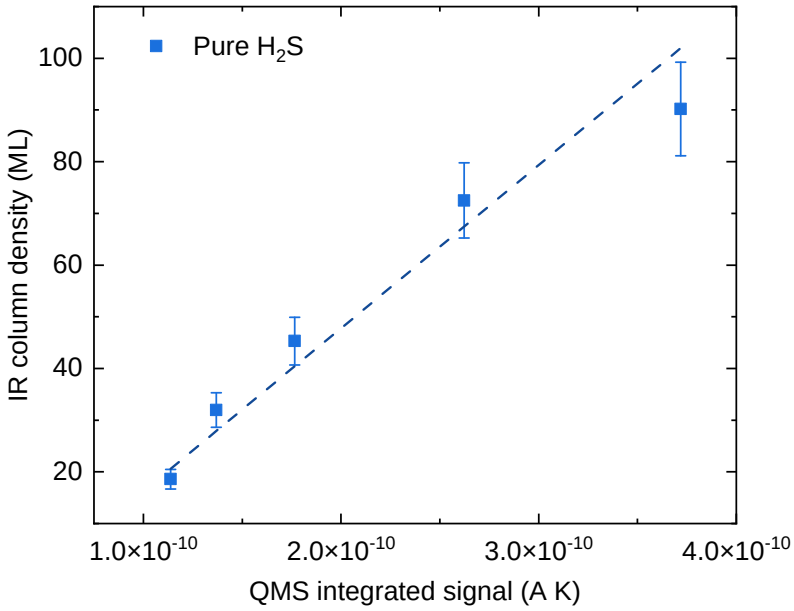

Figure 5.9: H_2S column densities derived from the integrated absorbance of its S-H stretching modes at 15 K for each multilayer ice thickness as a function of its corresponding integrated desorption feature as measured by the QMS. The dashed blue line shows the linear fit to the points from which the QMS-to-column density scaling factor was derived.

5.7.3 Arrhenius plots

Figure 5.11 shows the Arrhenius plots of the TPD experiments of all multilayer H_2S ice coverages. The desorption rate data (gray) for all five thicknesses was fit simultaneously following a Monte-Carlo sampling approach with 10,000 trials. The mean best-fit model corresponds to an H_2S-H_2S binding energy of $E_b = 3159 \pm 46$ K (blue dashed lines).

5.7.4 Multilayer H_2S ice fits with a temperature-dependent ν_{TST}

Figures 5.12 and 5.13 show the fits to the log-transformed multilayer TPD curves of H_2S with a temperature-dependent ν_{TST}. The former presents the data as the original TPD profile, while the latter shows the corresponding Arrhenius plots. This approach yields $E_b = 3141 \pm 49$ K (blue dashed lines).

5.7.5 Submonolayer fit with a single energy component

Figure 5.14 illustrates an attempted fit of the 0.2 ML H_2S ice using the Polanyi-Wigner equation (eq. 5.3) with a single temperature component. The fit fails to capture the experimental data, highlighting the presence of a distribution of binding energies caused by the inherent inhomogeneity of the cASW substrate.

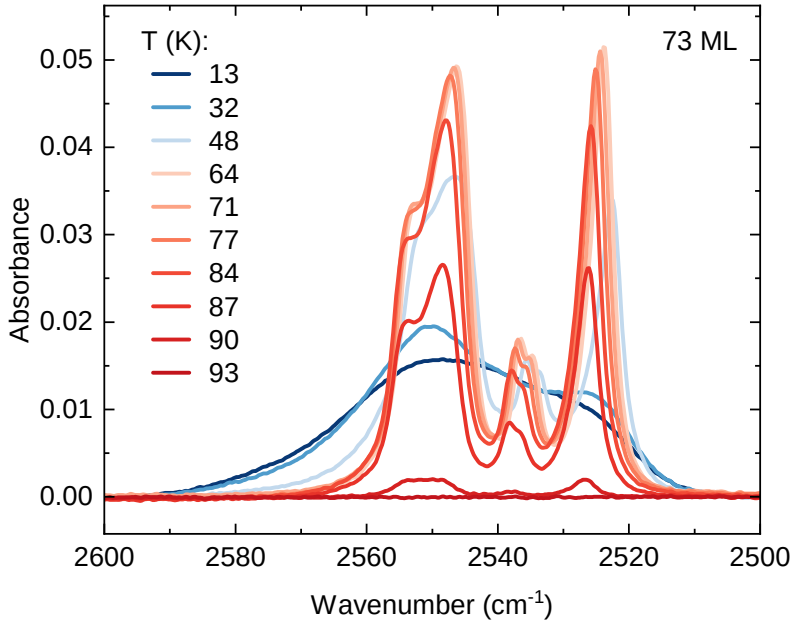

Figure 5.10: Infrared spectra taken during the TPD experiment of the 73 ML H_2S ice, centered on the frequency range of its S-H stretching modes. For clarity, only a subset of spectra collected at the relevant temperatures are shown.

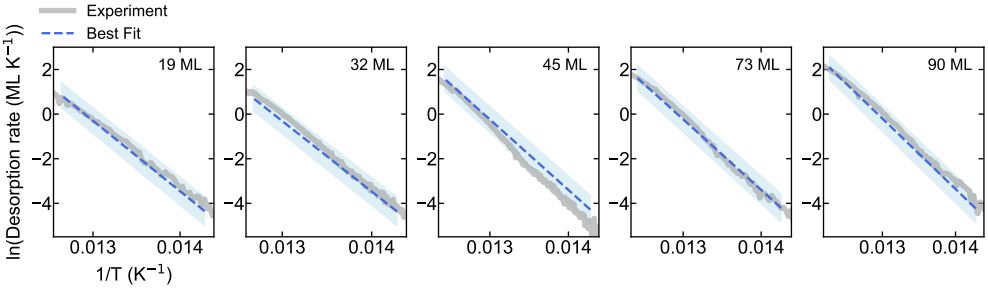

Figure 5.11: Arrhenius plots of the multilayer H_2S TPD curves used to derive the $H_2S{-}H_2S$ binding energy. The experimental data is shown in gray, while the linear fits to the plots, performed simultaneously for the five ice thicknesses, are shown by the blue dashed lines. The shaded blue region indicates the 1σ uncertainty. The fit is performed for the temperature range where the original curve follows an exponential trend (see section 5.3.1.1).

5.7.6 QMS-TPD results for mixed H_2O:H_2S ices

Figure 5.15 presents the QMS data collected for m/z = 34 during the TPD experiments with mixed H_2O:H_2S ices. In all cases, the first desorption feature (panel a) corresponds to monolayer desorption characterized by the $H_2S{-}H_2O$ binding energies. This is evinced by the peak desorption temperatures, which increase with decreasing coverages, and by the desorption profiles consistent with first-order desorption kinetics for all mixing ratios. The second desorption feature (panel b) corresponds to the molecular volcano.

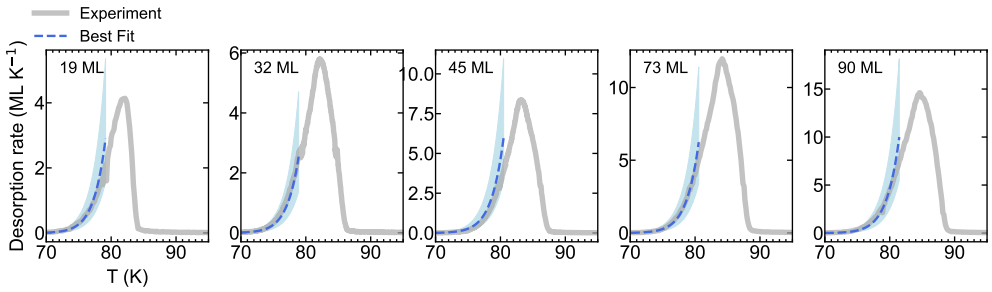

Figure 5.12: Same as Figure 5.2, but with fits performed using a temperature-dependent ν_{TST}.

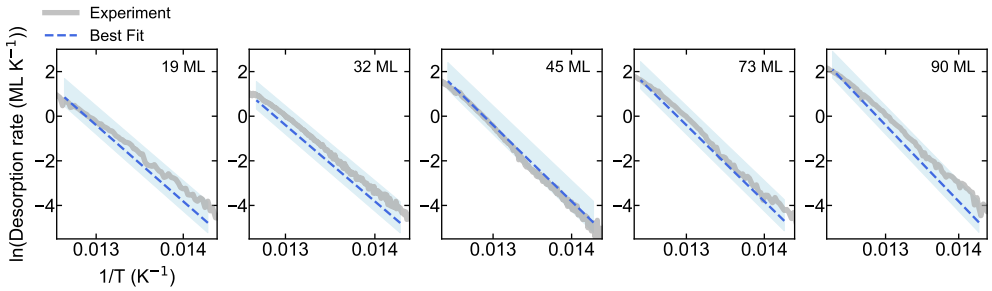

Figure 5.13: Same as Figure 5.11, but with fits performed using a temperature-dependent ν_{TST}.

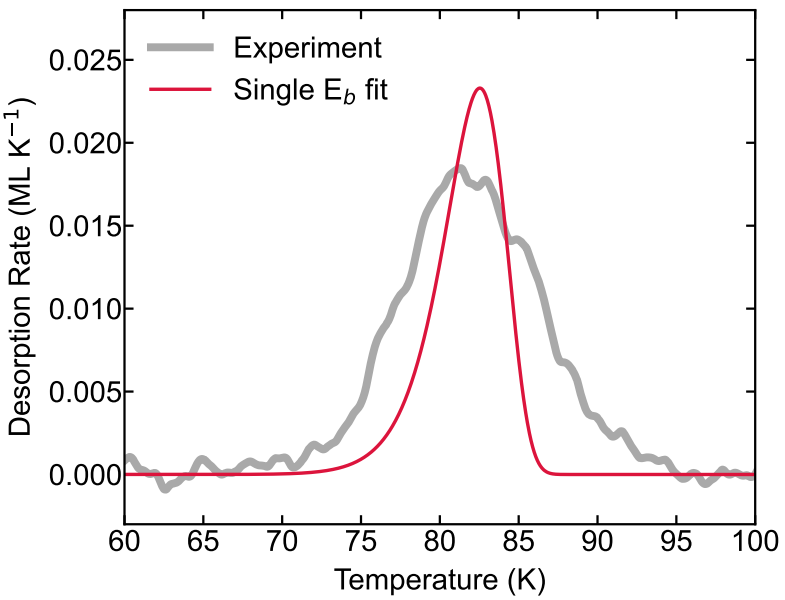

Figure 5.14: TPD curve of the 0.2 ML H_2S ice experiment deposited on top of a cASW substrate. The experimental data is show in gray, while the attempted fit to the data with a first-order Polanyi-Wigner curve with only one temperature component is shown in red.

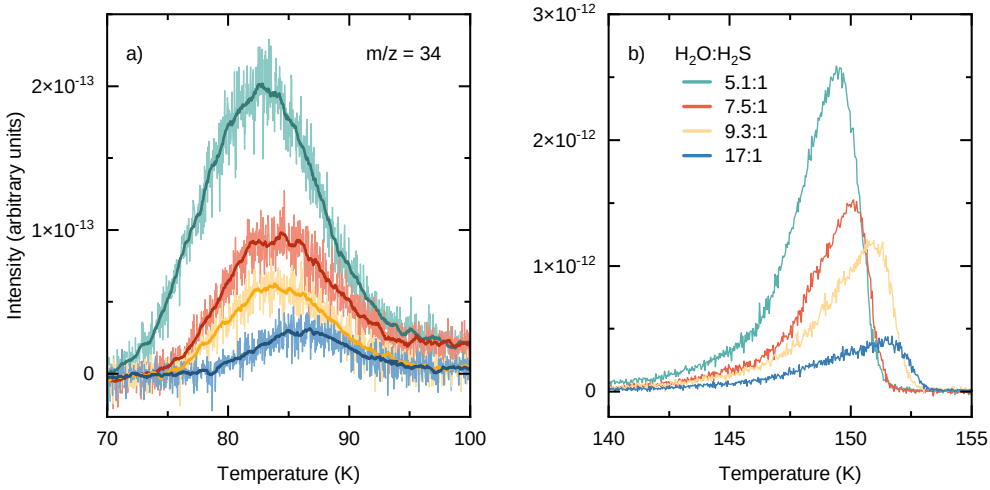

Figure 5.15: TPD data measured by the QMS for m/z = 34 in the experiments with mixed H_2O:H_2S ices. Panel a shows the monolayer desorption of H_2S molecules with access to the surface, and panel b depicts the molecular volcano feature due to H_2S entrapped in the H_2O ice matrix.